

## Visualizing Carrier Diffusion in Individual Single-Crystal Organolead Halide Perovskite Nanowires and Nanoplates

Wenming Tian,<sup>†</sup> Chunyi Zhao,<sup>†,‡</sup> Jing Leng,<sup>†</sup> Rongrong Cui,<sup>†</sup> and Shengye Jin<sup>\*,†</sup><sup>†</sup>State Key Laboratory of Molecular Reaction Dynamics, Dalian Institute of Chemical Physics, Chinese Academy of Sciences, 457 Zhong Shan Rd., Dalian, China, 116023<sup>‡</sup>School of Physics and Optoelectronic Engineering, Dalian University of Technology, 2 Ling Gong Rd., Dalian, China, 116024

## S Supporting Information

**ABSTRACT:** Single-crystal  $\text{CH}_3\text{NH}_3\text{PbX}_3$  ( $\text{X} = \text{I}^-$ ,  $\text{Cl}^-$ ,  $\text{Br}^-$ ) perovskite nanowires (NWs) and nanoplates (NPs), which demonstrate ultracompact sizes and exceptional photophysical properties, offer promises for applications in nanoscale photonics and optoelectronics. However, traditional electronic and transient techniques are limited by the dimensions of the samples, and characterizations of the carrier behavior (diffusion coefficient, charge mobility and diffusion length) in these NWs and NPs are extremely difficult. Herein, we report the direct visualization of the carrier diffusion process in individual single-crystal  $\text{CH}_3\text{NH}_3\text{PbI}_3$  and  $\text{CH}_3\text{NH}_3\text{PbBr}_3$  NWs and NPs using time-resolved and photoluminescence-scanned imaging microscopy. We report the diffusion coefficient (charge motility), which varies significantly between different NWs and NPs, ranging from  $1.59$  to  $2.41 \text{ cm}^2 \text{ s}^{-1}$  ( $56.4$  to  $93.9 \text{ cm}^2 \text{ V}^{-1} \text{ s}^{-1}$ ) for  $\text{CH}_3\text{NH}_3\text{PbI}_3$  and  $0.50$  to  $1.44 \text{ cm}^2 \text{ s}^{-1}$  ( $19.4$  to  $56.1 \text{ cm}^2 \text{ V}^{-1} \text{ s}^{-1}$ ) for  $\text{CH}_3\text{NH}_3\text{PbBr}_3$  and find this variation is independent of the shape and size of the sample. The average diffusion length is  $14.0 \pm 5.1 \mu\text{m}$  for  $\text{CH}_3\text{NH}_3\text{PbI}_3$  and  $6.0 \pm 1.6 \mu\text{m}$  for  $\text{CH}_3\text{NH}_3\text{PbBr}_3$ . These results provide information that is essential for the practical applications of the single-crystal perovskite NWs and NPs, and the imaging microscopy may also be applicable to other optoelectronic materials.

Single-crystal organolead halide  $\text{CH}_3\text{NH}_3\text{PbX}_3$  ( $\text{X} = \text{I}^-$ ,  $\text{Cl}^-$ ,  $\text{Br}^-$ ) perovskite nanowires (NWs) and nanoplates (NPs), mirroring the rapid development in photovoltaics from this class of semiconductor material,<sup>1–8</sup> have been also reported as an ideal candidate for applications in nanophotonics and nanoscale optoelectronics.<sup>9–14</sup> An example is the recent development of single-crystal perovskite NW and NP lasers that have shown very low lasing thresholds and high quality factors.<sup>11,12</sup> As in the remarkable performance of perovskites thin films in solar cells, the successful integration of perovskite nanostructured units in devices also critically depends on their important photophysical properties including the charge mobility (or diffusion coefficient) and carrier lifetimes;<sup>11,12,14</sup> a combination of these two parameters determines the carrier diffusion length. Therefore, in evaluating the quality of the perovskite NWs and NPs, quantitative characterizations on the behavior of charge carriers are very essential. The carrier lifetimes can be measured by time-resolved photoluminescence (PL);<sup>15–17</sup> however, determining

the charge mobility or diffusion coefficient normally requires perovskite samples with dimensions large enough to enable the deposition of electrodes or to obtain detectable spectroscopic signals. Limited by the sizes of samples, the traditional techniques such as time-of-flight,<sup>18,19</sup> Hall effect,<sup>18,20</sup> dark current–voltage,<sup>19,21</sup> PL quenching,<sup>5,22</sup> and transient spectroscopy<sup>23–25</sup> are not practical for measuring the diffusion coefficient and charge mobility of individual perovskite NWs and NPs. Therefore, these key photophysical properties and how they differ from the bulk crystal or between different NWs and NPs are still unknown.

Herein, we report the direct visualization and quantitative characterization of the carrier diffusion process in individual single-crystal  $\text{CH}_3\text{NH}_3\text{PbI}_3$  and  $\text{CH}_3\text{NH}_3\text{PbBr}_3$  NWs and NPs using time-resolved and PL-scanned imaging microscopy (Figure 1a). The details about the microscopy are in the Supporting Information (SI). Conceptually similar to previously reported PL and transient absorption imaging methods,<sup>26–28</sup> the measurement in this work is based on the diffusion of charge carriers after excitation pulse from an excitation spot ( $\sim 0.6 \mu\text{m}$  in radius) to a

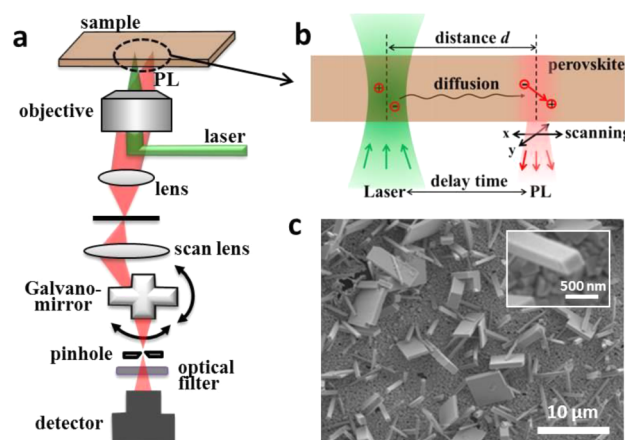


**Figure 1.** (a) PL-scanned confocal microscopy for visualizations of the charge carrier diffusion in single-crystal perovskite NWs and NPs. (b) A schematic presentation of the charge carrier excitation, diffusion, and recombination processes in perovskites. (c) A SEM image of as-grown single-crystal  $\text{CH}_3\text{NH}_3\text{PbI}_3$  NWs and NPs. The inset is an extended view of a NW.

Received: July 31, 2015

Published: September 21, 2015

different position where the change of carrier density can be monitored by the time-resolved PL as a function of delay time (Figure 1b). The diffusion parameters (diffusion coefficient, charge mobility and recombination constants) can be extracted from the fits of the PL kinetics by a diffusion model. The key part of the imaging microscopy is the use of a galvano-mirror in the PL collection pathway; by rotating this mirror the PL collection spot will scan over the whole sample with a fixed excitation position; this then constructs a PL intensity image that reflects the spatial distribution of charge carriers in the perovskite sample. The delay time between the excitation and emitting photons is recorded by the time-correlated single photon counting model. The lateral resolution of the measurement is determined by the optical diffraction limit ( $\sim 500$  nm for  $\text{CH}_3\text{NH}_3\text{PbI}_3$  and  $\sim 400$  nm for  $\text{CH}_3\text{NH}_3\text{PbBr}_3$ , see SI for details), making the imaging system very suitable for direct visualization of carrier diffusion in the perovskite NWs and NPs with a lateral dimension of a few micrometers.

We synthesize the single-crystal  $\text{CH}_3\text{NH}_3\text{PbI}_3$  and  $\text{CH}_3\text{NH}_3\text{PbBr}_3$  NWs and NPs by following the previously reported methods (see SI for details).<sup>9,11</sup> The lengths of NWs or side lengths of NPs are 5–20  $\mu\text{m}$  (see scanning electron microscopy (SEM) images in Figures 1c and S1). The thicknesses of NPs or the widths of rectangular cross-section of NWs vary between different particles and are typically a few hundreds of nanometers. Structural characterizations confirm the high quality and pure tetragonal (for  $\text{CH}_3\text{NH}_3\text{PbI}_3$ ) and cubical (for  $\text{CH}_3\text{NH}_3\text{PbBr}_3$ ) crystal structures of the perovskites without any impurities (Figure S1).<sup>9,11</sup> We also examine the photostability of the perovskite crystals, and no significant photodegradation is observed within 22 h under ambient condition (Figure S3).

The optical image of a typical  $\text{CH}_3\text{NH}_3\text{PbI}_3$  NP on a glass coverslip is shown in Figure 2a, where the red spot indicates the excitation position on the sample ( $\lambda_{\text{exc.}} = 680$  nm, 1 MHz,  $5.3 \mu\text{J}/\text{cm}^2/\text{pulse}$ ). We purposely excite the sample at the corner of the NP to allow for a larger space (longer distance) for carriers to diffuse (see Figure S2 for an example with the excitation at the center of a NP). By scanning the PL detection (760–840 nm) we obtain the PL intensity image (Figure 2b), which shows the PL signals not only from the excitation site but also from the whole crystal surface without direct excitation (see SI for details). Note that this PL image is integrated within the entire delay time window, and its time evolution process is shown in Figure S4.

Given this PL image, the change of PL intensity as a function of delay time (relative to the excitation pulse) can be easily extracted at any positions on the NP. In Figure 2c we compare PL kinetics collected at the excitation site and a position (position A in Figure 2b) with a distance of  $\sim 6 \mu\text{m}$  to the excitation site (see SI for the determination of distance). Unlike at the excitation site, the PL kinetics at position A includes a fast decay component right after the excitation (at  $t = 0$ ) and a clear slow rising and decay component at later time. If the PL at the position A is only from the charge carriers that diffuse to this position, the intensity should be zero at  $t = 0$  when charge carriers have not yet started to diffuse; we therefore attribute the fast decay component in the early time to the leaking of the wave-guided (WG) photons specifically those emitted from the excitation site (where the decay begins immediately after the excitation). However, because photons emitted from positions other than the excitation site can also be guided to A, we use the total PL decay collected from the whole NP to estimate the WG component. The comparison in Figure 2c indicates that the WG component can be well

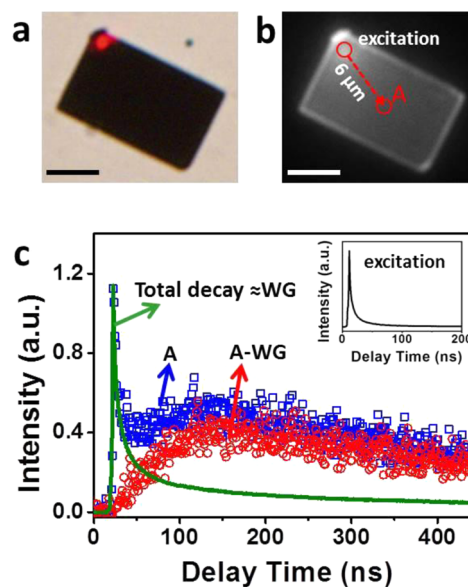


**Figure 2.** Optical (a) and PL intensity (b) images of a single-crystal  $\text{CH}_3\text{NH}_3\text{PbI}_3$  NP. The red spot in (a) is the excitation laser spot. The “A” (with a distance of  $\sim 6 \mu\text{m}$  to the excitation site) indicates the position where the PL kinetics is extracted for comparison. Bars are 5  $\mu\text{m}$ . (c) PL kinetics collected from the position A (blue squares) and the excitation site (inset). Solid green line is PL decay curve collected from the whole NP and is used to estimate the WG component (normalized at  $t = 0$ ) for subtraction. Red circles represent the kinetics at position A after subtracting the WG component.

described by the total PL decay (also see Figure S5 for comparisons at different diffusion distances). Subtraction of the WG component then yields the PL kinetics that is purely due to the charge carrier diffusion and recombination (Figure 2c) for a diffusion distance of 6  $\mu\text{m}$ .

This PL kinetics at the examined position reflects the change of carrier density as a function of time, which can be described by a two-dimensional diffusion model:

$$\frac{\partial \phi(x, y, t)}{\partial t} = D \left\{ \frac{\partial^2 \phi(x, y, t)}{\partial x^2} + \frac{\partial^2 \phi(x, y, t)}{\partial y^2} \right\} + f(\phi(x, y, t)) \quad (1)$$

$$f(\phi(x, y, t)) = -k_1 \phi(x, y, t) - k_2 \phi(x, y, t)^2 \quad (2)$$

where  $\phi(x, y, t)$  is the concentration of charge carriers at time  $t$  at the position  $(x, y)$  ( $0 \leq x \leq L_x$ ,  $0 \leq y \leq L_y$ ;  $L_x$  and  $L_y$  are side lengths of the crystal);  $D$  is the diffusion coefficient.  $f(\phi(x, y, t))$  is the charge recombination function,<sup>15–17,24,29,30</sup> where  $k_2$  is the radiative electron–hole recombination rate constant and  $k_1$  is defect-induced nonradiative carrier trapping rate constant. Using above equations, the carrier density at a delay time  $t$  at any positions on the sample can be simulated. The PL intensity  $I_{\text{PL}}(x, y, t)$  is then proportional to  $k_2 \phi(x, y, t)^2$ . Further details (boundary conditions and initial carrier distribution after excitation) about the simulation are available in SI. Fitting the PL kinetics with the diffusion model then yields the diffusion coefficient  $D$  and the recombination rate constants.

Figure 3 presents the measurements of a few typical  $\text{CH}_3\text{NH}_3\text{PbI}_3$  and  $\text{CH}_3\text{NH}_3\text{PbBr}_3$  NWs and NP (more measurements are shown in Figure S6). From the PL intensity images, we obtained a set of PL kinetics collected at various diffusion distances. Because the time-dependent carrier distribution is

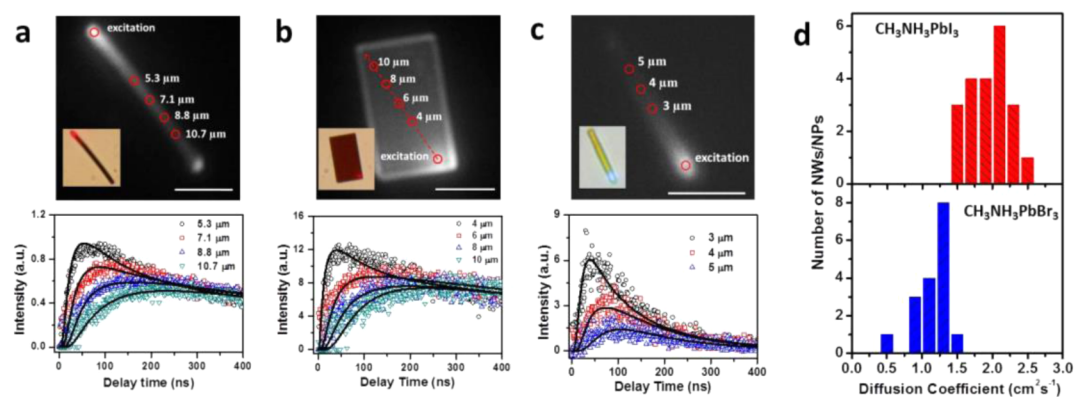


**Figure 3.** PL intensity images (upper panels) and a set of PL kinetics collected at different diffusion distances (lower panels) of a  $\text{CH}_3\text{NH}_3\text{PbI}_3$  NW (a) and NP (b) and a  $\text{CH}_3\text{NH}_3\text{PbBr}_3$  NW (c). Bars are 5  $\mu\text{m}$ . Insets are their optical images where the red and blue spots are the excitation laser spots (680 nm and  $5.3 \mu\text{J}/\text{cm}^2/\text{pulse}$  for (a) and (b); 450 nm and  $3.1 \mu\text{J}/\text{cm}^2/\text{pulse}$  for (c)). The red circles indicate the positions and diffusion distances where the PL kinetics is extracted. Black solid lines are the fits of the PL kinetics by the diffusion model discussed in the main text. The fitting parameters are summarized in Table 1. (d) Distribution histograms of the measured diffusion coefficients for dozens of  $\text{CH}_3\text{NH}_3\text{PbI}_3$  and  $\text{CH}_3\text{NH}_3\text{PbBr}_3$  NWs and NPs.

governed by eq 1, the PL kinetics at different position can be fit globally with  $D$ ,  $k_1$ , and  $k_2$  as the free fitting parameters. The experimental data are fit well by the diffusion model (Figure 3), and the fitting parameters are summarized in Table 1 (fitting parameters for more NWs and NPs are shown in Table S1).

**Table 1.** Fitting Parameters of the Perovskite NWs and NP Shown in Figure 3a–c<sup>a</sup>

	$D$ ( $\text{cm}^2 \text{s}^{-1}$ )	$k_1$ ( $\text{s}^{-1}$ ) $\times 10^6$	$k_2$ ( $\text{cm}^3 \text{s}^{-1}$ ) $\times 10^{-11}$	$\mu$ ( $\text{cm}^2 \text{V}^{-1} \text{s}^{-1}$ )
a	$2.05 \pm 0.02$	$0.82 \pm 0.02$	$3.76 \pm 0.26$	$79.7 \pm 0.7$
b	$1.65 \pm 0.03$	$0.77 \pm 0.03$	$8.24 \pm 0.69$	$64.1 \pm 1.0$
c	$0.88 \pm 0.03$	$2.53 \pm 0.10$	$19.5 \pm 0.10$	$34.2 \pm 0.7$

<sup>a</sup>Charge mobility is calculated from the diffusion coefficient.

Because the measurement of diffusion coefficient is based on the PL, the measured  $D$  should be an ambipolar diffusion coefficient. However, a recent study have shown that the exciton binding energy is only a few millielectronvolts in  $\text{CH}_3\text{NH}_3\text{PbI}_3$  perovskite at room temperature.<sup>31</sup> This confirms that the major charge carriers are free electrons and holes. Moreover, previous studies have demonstrated balanced diffusion lengths of electron and hole transport,<sup>5,22,23,32</sup> which means that the diffusion coefficient is similar for electron and hole. Correspondingly, the theoretical calculations and transient terahertz conductivity measurements also suggested comparable charge mobility for electron and hole in  $\text{CH}_3\text{NH}_3\text{PbI}_3$  perovskite.<sup>23,33</sup> Therefore, we speculate that the  $D$  measured here should represent the property of free electrons and holes ( $D_{\text{measured}} \approx D_e \approx D_h$ ) in the perovskite single crystals. The charge mobility ( $\mu$ ) of electron and hole can then be estimated via  $\mu = D \cdot e / (k_B T)$  by simply assuming  $\mu_e \approx \mu_h$ , where  $k_B$  is the Boltzmann's constant;  $T$  is the temperature; and  $e$  is the electronic charge.

Statistical examination from dozens of NWs and NPs for each type of perovskite provides a distribution of diffusion coefficient (Figure 3d). We find that  $D$  varies between different NWs and NPs synthesized under the same experiment condition, ranging from 1.59 to 2.41  $\text{cm}^2 \text{s}^{-1}$  for  $\text{CH}_3\text{NH}_3\text{PbI}_3$  and 0.50 to 1.44  $\text{cm}^2 \text{s}^{-1}$  for  $\text{CH}_3\text{NH}_3\text{PbBr}_3$ . The charge mobility is then calculated to be 56.4–93.9  $\text{cm}^2 \text{V}^{-1} \text{s}^{-1}$  for  $\text{CH}_3\text{NH}_3\text{PbI}_3$  and 19.4–56.1  $\text{cm}^2 \text{V}^{-1} \text{s}^{-1}$  for  $\text{CH}_3\text{NH}_3\text{PbBr}_3$ . We also find that the distributions of  $D$  for NWs and NPs are very similar and are not correlated to the

surface area or side length of particle (see Figure S7). This suggests that the diffusion coefficient should be independent of the shape and size of the single crystal. The variation in  $D$  may hint that the quality of the NPs and NWs probably highly depends on their local environments during their growth. As a result, for practical applications a prescreening examination of NWs and NPs is very necessary to guarantee a consistent performance for the devices. Nevertheless, the measured diffusion coefficient and charge mobility of the NWs and NPs by this imaging microscopy are within the range of reported values measured in bulk perovskite single crystals by time-of-flight or dark  $I$ – $V$  techniques,<sup>18,19,21</sup> confirming the capability of the imaging microscopy and the diffusion model for determining the diffusion coefficient and charge mobility.

The fitting of the PL kinetics also yields the charge recombination rate constants (see Tables 1 and S1). The charge recombination model assumes that the trapping rate constant is similar for electron and hole. This assumption is justified by the reported balanced charge mobility and similar trap density of electron and hole in the perovskites.<sup>18,23</sup> The bimolecular rate constant  $k_2$  measured here for  $\text{CH}_3\text{NH}_3\text{PbI}_3$  NWs and NPs is consistent with that reported in literatures for the polycrystalline thin films,<sup>24,34,35</sup> whereas the nonradiative trapping rate  $k_1$  is smaller by almost 2 orders of magnitude,<sup>15,17</sup> confirming that the perovskite single crystals have much lower defect densities.<sup>18,19,21</sup> To further confirm the accuracy of the measured recombination constants, we also perform the excitation intensity-dependent measurement (Figure S8), which shows consistent results under different laser intensities.

With a given carrier diffusion coefficient, the carrier diffusion length ( $L_D$ ) can be calculated via  $L_D = (D\tau)^{1/2}$ , where  $\tau$  is the carrier lifetime. It is known that high excitation intensity can reduce the carrier diffusion length by increasing the bimolecular recombination. At extremely low excitation intensity (or carrier density), the carrier recombination is dominated by the trapping of carriers, and the lifetime can be estimated by  $1/k_1$ . Using the  $D$  and  $k_1$  data in Table S1, we estimate the upper limit of carrier diffusion length of the examined NWs and NPs and obtain the average  $L_D$  of  $14.0 \pm 5.1 \mu\text{m}$  for  $\text{CH}_3\text{NH}_3\text{PbI}_3$  and  $6.0 \pm 1.6 \mu\text{m}$  for  $\text{CH}_3\text{NH}_3\text{PbBr}_3$ . Recently a record diffusion length up to 175  $\mu\text{m}$  has been reported in bulk  $\text{CH}_3\text{NH}_3\text{PbI}_3$  single crystal.<sup>18</sup> Compared to our results, such longer diffusion length is due to



the longer carrier lifetime up to 82–95  $\mu$ s. This suggests that there may be room to further improve the diffusion length in these single-crystal NWs and NPs through the optimization of the synthesis and/or passivation of surface defects.<sup>36,37</sup>

In summary, we have demonstrated the successful measurements of carrier diffusion coefficient, charge mobility, recombination rate constants, and carrier diffusion length in individual single-crystal  $\text{CH}_3\text{NH}_3\text{PbI}_3$  and  $\text{CH}_3\text{NH}_3\text{PbBr}_3$  NWs and NPs through the direct imaging of carrier diffusion process using the time-resolved and PL-scanned imaging microscopy. The quantitative determinations of these important photophysical parameters are essential for the practical applications of single-crystal perovskite NWs and NPs. This imaging system not only explores the intrinsic properties about carrier diffusion but also can serve as a tool for fast quality screening for perovskite nanostructures and should be also applicable to other optoelectronic materials.

## ■ ASSOCIATED CONTENT

### ● Supporting Information

The Supporting Information is available free of charge on the ACS Publications website at DOI: 10.1021/jacs.5b08045.

Experimental setup; synthesis of samples; structural characterizations; simulation of carrier diffusion; additional results of measurements (PDF)

## ■ AUTHOR INFORMATION

### Corresponding Author

\*sjin@dicp.ac.cn

### Notes

The authors declare no competing financial interest.

## ■ ACKNOWLEDGMENTS

The authors acknowledge the funding support from State Key Laboratory of Molecular Reaction Dynamics at Dalian Institute of Chemical Physics of Chinese Academy of Sciences and National Nature Science Foundation of China (Grant 21473192).

## ■ REFERENCES

- (1) Kojima, A.; Teshima, K.; Shirai, Y.; Miyasaka, T. *J. Am. Chem. Soc.* **2009**, *131*, 6050.
- (2) Chen, Q.; Zhou, H.; Hong, Z.; Luo, S.; Duan, H. S.; Wang, H. H.; Liu, Y.; Li, G.; Yang, Y. *J. Am. Chem. Soc.* **2014**, *136*, 622.
- (3) Nie, W.; Tsai, H.; Asadpour, R.; Blancon, J. C.; Neukirch, A. J.; Gupta, G.; Crochet, J. J.; Chhowalla, M.; Tretiak, S.; Alam, M. A.; Wang, H. L.; Mohite, A. D. *Science* **2015**, *347*, 522.
- (4) Yang, B.; Dyck, O.; Poplawsky, J.; Keum, J.; Puzos, A.; Das, S.; Ivanov, I.; Rouleau, C.; Duscher, G.; Geohegan, D.; Xiao, K. *J. Am. Chem. Soc.* **2015**, *137*, 9210.
- (5) Stranks, S. D.; Eperon, G. E.; Grancini, G.; Menelaou, C.; Alcocer, M. J. P.; Leijtens, T.; Herz, L. M.; Petrozza, A.; Snaith, H. J. *Science* **2013**, *342*, 341.
- (6) Burschka, J.; Pellet, N.; Moon, S. J.; Humphry-Baker, R.; Gao, P.; Nazeeruddin, M. K.; Gratzel, M. *Nature* **2013**, *499*, 316.
- (7) Ahn, N.; Son, D. Y.; Jang, I. H.; Kang, S. M.; Choi, M.; Park, N. G. *J. Am. Chem. Soc.* **2015**, *137*, 8696.
- (8) Zhou, H. P.; Chen, Q.; Li, G.; Luo, S.; Song, T. B.; Duan, H. S.; Hong, Z. R.; You, J. B.; Liu, Y. S.; Yang, Y. *Science* **2014**, *345*, 542.
- (9) Fu, Y.; Meng, F.; Rowley, M. B.; Thompson, B. J.; Shearer, M. J.; Ma, D.; Hamers, R. J.; Wright, J. C.; Jin, S. *J. Am. Chem. Soc.* **2015**, *137*, 5810.
- (10) Zhu, F.; Men, L.; Guo, Y.; Zhu, Q.; Bhattacharjee, U.; Goodwin, P. M.; Petrich, J. W.; Smith, E. A.; Vela, J. *ACS Nano* **2015**, *9*, 2948.

- (11) Zhu, H.; Fu, Y.; Meng, F.; Wu, X.; Gong, Z.; Ding, Q.; Gustafsson, M. V.; Trinh, M. T.; Jin, S.; Zhu, X. Y. *Nat. Mater.* **2015**, *14*, 636.
- (12) Liao, Q.; Hu, K.; Zhang, H.; Wang, X.; Yao, J.; Fu, H. *Adv. Mater.* **2015**, *27*, 3405.
- (13) Im, J. H.; Luo, J.; Frankevicius, M.; Pellet, N.; Gao, P.; Moehl, T.; Zakeeruddin, S. M.; Nazeeruddin, M. K.; Gratzel, M.; Park, N. G. *Nano Lett.* **2015**, *15*, 2120.
- (14) Wong, A. B.; Lai, M.; Eaton, S. W.; Yu, Y.; Lin, E.; Dou, L.; A, F.; Yang, P. *Nano Lett.* **2015**, *15*, 5519.
- (15) Yamada, Y.; Nakamura, T.; Endo, M.; Wakamiya, A.; Kanemitsu, Y. *J. Am. Chem. Soc.* **2014**, *136*, 11610.
- (16) Stranks, S. D.; Burlakov, V. M.; Leijtens, T.; Ball, J. M.; Goriely, A.; Snaith, H. J. *Phys. Rev. Appl.* **2014**, *2*, 034007.
- (17) D'Innocenzo, V.; Kandada, A. R. S.; De Bastiani, M.; Gandini, M.; Petrozza, A. *J. Am. Chem. Soc.* **2014**, *136*, 17730.
- (18) Dong, Q.; Fang, Y.; Shao, Y.; Mulligan, P.; Qiu, J.; Cao, L.; Huang, J. *Science* **2015**, *347*, 967.
- (19) Shi, D.; Adinolfi, V.; Comin, R.; Yuan, M.; Alarousu, E.; Buin, A.; Chen, Y.; Hoogland, S.; Rothenberger, A.; Katsiev, K.; Losovyj, Y.; Zhang, X.; Dowben, P. A.; Mohammed, O. F.; Sargent, E. H.; Bakr, O. M. *Science* **2015**, *347*, 519.
- (20) Xiao, Z. G.; Dong, Q. F.; Bi, C.; Shao, Y. C.; Yuan, Y. B.; Huang, J. S. *Adv. Mater.* **2014**, *26*, 6503.
- (21) Saidaminov, M. I.; Abdelhady, A. L.; Murali, B.; Alarousu, E.; Maulakov, V. M.; Peng, W.; Dursun, L.; Wang, L.; He, Y.; Maculan, G.; Goriely, A.; Wu, T.; Mohammed, O. F.; Bakr, O. M. *Nat. Commun.* **2015**, *6*, 7586.
- (22) Sheng, R.; Ho-Baillie, A.; Huang, S. J.; Chen, S.; Wen, X. M.; Hao, X. J.; Green, M. A. *J. Phys. Chem. C* **2015**, *119*, 3545.
- (23) Ponseca, C. S.; Savenije, T. J.; Abdellah, M.; Zheng, K. B.; Yartsev, A.; Pascher, T.; Harlang, T.; Chabera, P.; Pullerits, T.; Stepanov, A.; Wolf, J. P.; Sundstrom, V. *J. Am. Chem. Soc.* **2014**, *136*, 5189.
- (24) Wehrenfennig, C.; Eperon, G. E.; Johnston, M. B.; Snaith, H. J.; Herz, L. M. *Adv. Mater.* **2014**, *26*, 1584.
- (25) Oga, H.; Saeki, A.; Ogomi, Y.; Hayase, S.; Seki, S. *J. Am. Chem. Soc.* **2014**, *136*, 16948.
- (26) Akselrod, G. M.; Deotare, P. B.; Thompson, N. J.; Lee, J.; Tisdale, W. A.; Baldo, M. A.; Menon, V. M.; Bulovic, V. *Nat. Commun.* **2014**, *5*, 3646.
- (27) Guo, Z.; Manser, J. S.; Wan, Y.; Kamat, P. V.; Huang, L. B. *Nat. Commun.* **2015**, *6*, 7471.
- (28) Gabriel, M. M.; Kirschbrown, J. R.; Christesen, J. D.; Pinion, C. W.; Zigler, D. F.; Grumstrup, E. M.; Mehl, B. P.; Cating, E. E. M.; Cahoon, J. F.; Papanikolas, J. M. *Nano Lett.* **2013**, *13*, 1336.
- (29) Manser, J. S.; Kamat, P. V. *Nat. Photonics* **2014**, *8*, 737.
- (30) Saba, M.; Cadelano, M.; Marongiu, D.; Chen, F. P.; Sarritzu, V.; Sestu, N.; Figus, C.; Aresti, M.; Piras, R.; Geddo, Lehmann, A.; Cannas, C.; Musinu, A.; Quochi, F.; Mura, A.; Bongiovanni, G. *Nat. Commun.* **2014**, *5*, 5049.
- (31) Miyata, A.; Mitioglu, A.; Plochocka, P.; Portugall, O.; Wang, J. T.-W.; Stranks, S. D.; Snaith, H. J.; Nicholas, R. J. *Nat. Phys.* **2015**, *11*, 582.
- (32) Xing, G. C.; Mathews, N.; Sun, S. Y.; Lim, S. S.; Lam, Y. M.; Gratzel, M.; Mhaisalkar, S.; Sum, T. C. *Science* **2013**, *342*, 344.
- (33) Giorgi, G.; Yamashita, K. *J. Mater. Chem. A* **2015**, *3*, 8981.
- (34) Deschler, F.; Price, M.; Pathak, S.; Klintberg, L. E.; Jarausch, D. D.; Högler, R.; Hüttner, S.; Leijtens, T.; Stranks, S. D.; Snaith, H. J.; Atature, M.; Phillips, R. T.; Friend, R. H. *J. Phys. Chem. Lett.* **2014**, *5*, 1421.
- (35) deQuilettes, D. W.; Vorpahl, S. M.; Stranks, S. D.; Nagaoka, H.; Eperon, G. E.; Ziffer, M. E.; Snaith, H. J.; Ginger, D. S. *Science* **2015**, *348*, 683.
- (36) Abate, A.; Saliba, M.; Hollman, D. J.; Stranks, S. D.; Wojciechowski, K.; Avolio, R.; Grancini, G.; Petrozza, A.; Snaith, H. J. *Nano Lett.* **2014**, *14*, 3247.
- (37) Noel, N. K.; Abate, A.; Stranks, S. D.; Parrott, E. S.; Burlakov, V. M.; Goriely, A.; Snaith, H. J. *ACS Nano* **2014**, *8*, 9815.